FLEXIBLE HYDROFOIL OPTIMIZATION FOR THE 35th AMERICA'S CUP WITH CONSTRAINED EGO METHOD

M. Sacher, Naval Academy Research Institute, France, matthieu.sacher@ecole-navale.fr
M. Durand, K-Epsilon, Groupama Team France, Sirli Innovations, France
E. Berrini, MyCFD, France
F. Hauville, Naval Academy Research Institute, France
R. Duvigneau, Université Côte d'Azur, INRIA, CNRS, France
O. Le Maître, LIMSI - CNRS, France
J. A. Astolfi, Naval Academy Research Institute, France

This paper investigates the use of constrained surrogate models to solve the multi-design optimization problem of a flexible hydrofoil. The surrogate-based optimization (EGO) substitutes the complex objective function of the problem by an easily evaluable model, constructed from a limited number of computations at carefully selected design points. Associated with ad-hoc statistical strategies to propose optimum candidates within the estimated feasible domain, EGO enables the resolution of complex optimization problems. In this work, we rely on Gaussian processes (GP) to model the objective function and adopt a probabilistic classification method to treat non-explicit inequality constraints and non-explicit representation of the feasible domain. This procedure is applied to the design of the shape and the elastic characteristics of a hydrofoil equipped with deformable elements providing flexibility to the trailing edge. The optimization concerns the minimization of the hydrofoil drag while ensuring a non-cavitating flow, at selected sailing conditions (boat speed and lifting force). The drag value and cavitation criterion are determined by solving a two-dimensional nonlinear fluid-structure interaction problem, based on a static vortex lattice method with viscous boundary layer equations, for the flow, and a nonlinear elasticity solver for the deformations of the elastic components of the foil. We compare the optimized flexible hydrofoil with a rigid foil geometrically optimized for the same sailing conditions. This comparison highlights the hydrodynamical advantages brought by the flexibility: a reduction of the drag over a large range of boat speeds, less susceptibility to cavitation and a smaller angle of attack tuning range.

1 INTRODUCTION

Created in 1851, the America's Cup trophy is one of the oldest international sports competition. The race opposes two sailing boats, representing a defender and a challenger yacht clubs, that race one against the other to be the winner of the America's Cup match races. In each edition, specific rules are provided by the defender in accordance with the *Deed of Gift*, which define the format of the regatta, the location of the races and restrictions on the type of boats allowed to compete. When a challenging yacht club wins the match races, it becomes the defender and gains the stewardship for the next America's Cup edition.

The 35^{th} edition, to take place in June 2017, will be raced on so-called AC50s catamarans with size fixed to 50 feet, equipped with hydrofoils and wing-sails. The hydrofoils are expected to be a key component of the AC50s performance, and the competing teams are dedicating a growing fraction of their design effort to their optimization in comparison to older yacht design approach [36]. The optimization aims at designing hydrofoil with a minimal drag force over a whole range of boat speeds (BS), while ensuring a sufficient lift force for the boat to fly, especially at the lowest BS. The design of the hydrofoil is restricted by the "AC Class Rule" documents. In particular, the rule number 11.11 states: *"Daggerboard components shall be rigidly fixed to each other and the daggerboard shape shall not be adjusted while racing."* One possible way to comply with this rule, while allowing for some adaptivity of the shape with the BS, is to design a hydrofoil composed of rigidly mounted components, undergoing large elastic deformations under the hydrodynamical loads and without crew adjustments. For instance, a reduction of the hydrofoil camber, with increasing BS and hydrodynamic loads, can be obtained using a flexible trailing edge.

Drag reduction by shape optimization is an important research topic, with many applications in domains ranging from aeronautic to wind-energy recovery. Multiple studies have been proposed, based on physical models with different levels of complexity. For instance, the geometrical optimization of an airfoil with a two-dimensional steady flow model is considered in [35] when the unsteady flow situation is treated in [41]. Complex optimizations for a range of Mach numbers of a two-dimensional airfoil have been performed by [24], and the robust optimization for uncertain flows and geometries is

considered in [29]. The numerical optimization of hydrofoils is to our knowledge much rarer, and the hydrofoil literature generally focuses on the stability [18], wake energy reduction [21], and free surface elevation [14] aspects.

This paper reports the development and application, in partnership with the *Groupama Team France (GTF)* design team, of an Efficient Global Optimization (EGO) procedure tailored to the flexible hydrofoil optimization problem. We restrict ourselves to the optimization of a two-dimensional hydrofoil consisting of rigid forward and trailing parts, connected by a deformable element. The objective of the optimization is the reduction of the hydrodynamic drag at several BS and lift conditions, with cavitation constraints. Cavitation is indeed an important concern for the hydrofoil performance [39], but its numerical prediction remains a difficult problem, as shown for instance in [23, 9, 11, 2]. These difficulties explain that cavitation aspects are usually not considered in hydrofoil shape optimization, unless when the objective is precisely to delay the cavitation, such as in [47].

The optimization of flexible hydrofoils raises many challenges. First it requires multi-design variables to prescribe the foil geometry at rest (unloaded shape), on the one hand, and the elastic properties and the internal structure of the deformable parts, on the other hand. Second, the evaluation of the performance of a given design requires the resolution of a fully nonlinear fluid-structure interaction (FSI) problem, possibly combining different boat speeds, with a numerical cost that inherently limits the number of designs that can be evaluated. Finally, considering constraint on non-cavitating flow requires an appropriate treatment of constraints that are costly evaluate for a given design. As a matter of fact, the numerical optimization requires dedicated techniques to circumvent the computational complexity of the problem. In the present work, the numerical modeling involves the coupling of the two-dimensional vortex lattice method solver XFOIL [10], to compute the flow, with the structural ARA software developed by K-EPSILON [13], to compute the hydrofoil deformations. Even for this two-dimensional modeling, the computational times prevent the direct optimization based on the FSI solution with standard methods.

We then rely on a surrogate model to reduce the computational burden of optimizing complex systems with costly objective function estimation [40]. Specifically, we use Gaussian processes [22] surrogate models with Efficient Global Optimization (EGO) strategies [20], that have been previously applied to aerodynamic drag reduction [19], vibration reduction for rotating aircrafts [15], optimization of FSI problems [1] and sail trimming optimization [37]. The classification approach for discontinuous or binary constraints proposed in [6] is extended to the treatment of the cavitation constraints in the optimization procedure. In our approach, The admissible domain is approximated using Least-Squares Support Vector Machine (LS-SVM) [42] regression from the previous observations. An original contribution of the work is a new probabilistic treatment of the constraints which is designed to mitigate the risk of exploring unfeasible solutions (which yield a cavitating flow).

This optimization procedure used in the present work is briefly described in Section 2, while Section 3 discusses the formulation of the optimization problem for the flexible hydrofoil, including the definition of the optimization variables and a brief discussion of the numerical models. Section 4 presents the optimization results, emphasizing on impact of the flexibility of the performance of the optimal hydrofoil. In particular, these performances are contrasted with the case of a rigid hydrofoil optimized for the same conditions. We have tried to provide as much as possible quantitative results, but for confidentiality reasons related to the partnership with the GTF design team, some values can not be provided and only trends are reported. Finally, conclusions and recommendations for future development are given in Section 5.

2 GP-BASED CONSTRAINED OPTIMIZATION

The objective is to estimate the solution $\mathbf{x}_{\text{opt}}$ of the following abstract optimization problem

$$\min_{\mathbf{x}\in\Omega} \mathcal{P}(\mathbf{x}), \quad \text{s.t. } \mathbf{Q}(\mathbf{x}) \geq \mathbf{0},$$

where $\mathbf{x} \in \mathbb{R}^d$ is the vector of control variables, Ω the optimization domain, $\mathcal{P} : \Omega \mapsto \mathbb{R}$ the objective function and $\mathbf{Q} : \mathbf{x} \mapsto \mathbb{R}^m$ is the vector of constraints. Even in the unconstrained case, $m = 0$, finding the global optimum of $\mathcal{P}$ can be very costly, in particular when its evaluation is numerically expensive. The use of surrogate models for $\mathcal{P}$ is then a classical solution to reduce the computational burden of complex systems optimization [40]. We use Gaussian processes (GP) [22] which, owing to their statistical nature, provide both a prediction of the objective function and a measure of the uncertainty (variance) in the prediction. These features are appealing in optimization, as they can be used to derive rigorous optimization strategies based on the maximization of the Expected Improvement (EI) criterion, leading to methods referred globally as the Efficient Global Optimization (EGO) [20] methods. In Section 2.1 we review the construction of the GP model for $\mathcal{P}$ and the resulting optimization strategy in the unconstrained case. The constrained case is considered in Section 2.2.

2.1 UNCONSTRAINED EGO USING GP

Consider a set of n training inputs points $\mathbf{X}_n = \{\mathbf{x}_1, \ldots, \mathbf{x}_n\}$, each associated to a noisy observation y_i of the objective function. Specifically, it is assumed that $y_i = \mathcal{P}(\mathbf{x}_i) + \varepsilon_i$, where the ε_i are Gaussian measurement noises, assumed for simplicity independent and identically distributed with variance ${\sigma_\epsilon}^2$. The GP construction considers that $\mathcal{P}$ is a realization of a zero-mean multivariate Gaussian process with covariance function $C_{\mathcal{P}}$. In this work, we consider the multidimensional squared exponential covariance functions defined by

$$C_{\mathcal{P}}(\mathbf{x}, \mathbf{x}'; \boldsymbol{\Theta}) \doteq \theta_1 \prod_{i=1}^{d} \exp\left(\frac{-(x_i - x_i')^2}{2l_i^2}\right) + \theta_2, \qquad (1)$$

where $\boldsymbol{\Theta} = \{\theta_1, \theta_2, l_1, l_2, \ldots, l_d\}$ is a vector of hyperparameters to be inferred from the observations. Denoting $\mathbf{C}(\boldsymbol{\Theta}) \in \mathbb{R}^{n\times n}$ the covariance matrix with entries $C_{i,j}(\boldsymbol{\Theta}) \doteq$

$C_{\mathcal{P}}(\mathbf{x}_i, \mathbf{x}_j; \boldsymbol{\Theta})$, $1 \leq i, j \leq n$, the joint Gaussian distribution of the noisy observations vector, $\mathbf{Y}_n = (y_1, \ldots, y_n)^{\mathrm{T}}$, and the predicted observation $y(\mathbf{x})$ is given by

$$\begin{pmatrix} \mathbf{Y}_n \\ y(\mathbf{x}) \end{pmatrix} \sim \mathcal{N}\left(\mathbf{0}, \begin{bmatrix} \mathbf{C} + {\sigma_\epsilon}^2\mathbf{I} & \mathbf{k}(\mathbf{x}) \\ \mathbf{k}^{\mathrm{T}}(\mathbf{x}) & \kappa(\mathbf{x}) + {\sigma_\epsilon}^2 \end{bmatrix}\right). \quad (2)$$

In (2) we have denoted $\kappa(\mathbf{x}) \doteq C_{\mathcal{P}}(\mathbf{x}, \mathbf{x}; \boldsymbol{\Theta})$, $\mathbf{k}(\mathbf{x}) \doteq (C_{\mathcal{P}}(\mathbf{x}, \mathbf{x}_1; \boldsymbol{\Theta}) \cdots C_{\mathcal{P}}(\mathbf{x}, \mathbf{x}_n; \boldsymbol{\Theta}))^{\mathrm{T}}$ and $\mathbf{I}$ the identity matrix of $\mathbb{R}^n$. From the conditional rules of joint Gaussian distributions [34], the *best* prediction $\widehat{\mathcal{P}}_n(\mathbf{x})$ of $\mathcal{P}(\mathbf{x})$, *i.e.* the mean of y, and the prediction variance $\hat{\sigma}^2_{\mathcal{P}}(\mathbf{x})$ are given by

$$\widehat{\mathcal{P}}_n(\mathbf{x}) = \mathbf{k}^{\mathrm{T}}(\mathbf{x}) \left(\mathbf{C}(\boldsymbol{\Theta}) + {\sigma_\epsilon}^2\mathbf{I}\right)^{-1} \mathbf{Y}_n, \quad (3)$$

$$\hat{\sigma}^2_{\mathcal{P}}(\mathbf{x}) = \kappa(\mathbf{x}) + {\sigma_\epsilon}^2 - \mathbf{k}^{\mathrm{T}}(\mathbf{x}) \left(\mathbf{C}(\boldsymbol{\Theta}) + {\sigma_\epsilon}^2\mathbf{I}\right)^{-1} \mathbf{k}(\mathbf{x}). \quad (4)$$

The hyper-parameters $\boldsymbol{\Theta}$ and noise variance ${\sigma_\epsilon}^2$ can be determined by maximizing the log-marginal likelihood [34] using an evolution strategy algorithm [16]. More details on GP meta-models can be found in [34].

Let $\hat{\mathbf{x}}_n$ be the optimum of $\widehat{\mathcal{P}}_n(\mathbf{x})$. It is expected that $\hat{\mathbf{x}}_n \approx \mathbf{x}_{\mathrm{opt}}$ if the approximation error $\widehat{\mathcal{P}}_n - \mathcal{P}$ is small enough. The advantage of minimizing $\widehat{\mathcal{P}}_n$ instead of $\mathcal{P}$ is that GP models are usually inexpensive to evaluate compared to the original objective function. To control the error in the approximation, one proceeds sequentially by adding progressively new observation points in the area of interest. A deterministic optimization procedure would choose the next point $\mathbf{x}_{n+1}$ as the optimal point of $\widehat{\mathcal{P}}_n$. However, the GP model provides probabilistic information that can be exploited to propose more robust strategies based on merit functions, which combine the prediction and its variance. In this work, we use the Augmented Expected Improvement (AEI) merit function [17], which estimates the expected progress in the objective, taking into account the noise in the observed values and the prediction variance:

$$AEI(\mathbf{x}) = EI(\mathbf{x}) \left(1 - \frac{\sigma_\epsilon}{\sqrt{\hat{\sigma}^2_{\mathcal{P}}(\mathbf{x}) + {\sigma_\epsilon}^2}}\right), \quad (5)$$

where the Expected Improvement $EI(\mathbf{x})$ is defined by

$$EI(\mathbf{x}) = \hat{\sigma}^2_{\mathcal{P}}(\mathbf{x}) \left[u(\mathbf{x})\Phi\left(u(\mathbf{x})\right) + \phi\left(u(\mathbf{x})\right)\right], \quad (6)$$

$$u(\mathbf{x}) = \frac{\widehat{\mathcal{P}}_n(\mathbf{x}_{*,n}) - \widehat{\mathcal{P}}_n(\mathbf{x})}{\hat{\sigma}^2_{\mathcal{P}}(\mathbf{x})}, \quad (7)$$

with Φ and ϕ the cumulative and density functions of the standard Gaussian distribution, and $\mathbf{x}_{*,n} \in \mathbf{X}_n$ is the current effective best solution (see [17]). The optimum $\mathbf{x}_{n+1}$ of the AEI is added to $\mathbf{X}_n$, and $\mathcal{P}$ is evaluated at the new point providing y_{n+1}. Setting $n \leftarrow n + 1$, a new iteration can start updating the GP model with the new observation. Overall, each iteration requires one computation of the objective and the resolution of two optimization problems: a first one for the hyper-parameters of the GP model, and a second one to find the AEI optimum. The iterations of the GP-based optimization problem are continued until a stopping criterion is satisfied or the resources allocated to the optimization have been exhausted.

2.2 EGO UNDER CONSTRAINTS, A CLASSIFICATION BASED APPROACH

EGO methods with inequality constraints was considered in [38]. The key idea was to rely on m additional surrogates to estimate the constraints $Q_i(\mathbf{x})$. For Gaussian Process models, one can easily determine the probability $P_i(Q_i \geq 0|\mathbf{x})$ that a constraint Q_i is satisfied at $\mathbf{x}$ and, assuming the independence of the constraints probability, to come up with the consolidated probability $P(\mathbf{Q} \geq \mathbf{0}|\mathbf{x}) = \Pi_{i=1}^m P_i(Q_i \geq 0|\mathbf{x})$. This probability is used to modify the unconstrained AEI criterion and favor feasible regions:

$$AEI_{\mathbf{Q}}(\mathbf{x}) = AEI(\mathbf{x})P(\mathbf{Q} \geq \mathbf{0}|\mathbf{x}).$$

Although effective in many problems, this GP modeling of the constraints faces several limitations. First, its computational cost increases with the number m of constraints and can be an issue for problems with large m. Second, the approximation by GP models assumes a sufficient smoothness of the Q_i, which must be evaluable for almost every $\mathbf{x} \in \Omega$. This rules out the case of binary constraints (feasible / infeasible) and models having no solution for $\mathbf{Q}(\mathbf{x}) \not\geqslant \mathbf{0}$. Finally, the approach is also limited to situations where the feasible domain has an explicit representation in terms of the constraints. The optimization of hydrofoils reaches some of these limitations as it is difficult to express feasible geometries in terms of constraints on design parameters, while some values may lead to uncomputable solutions.

Classification methods recently proposed in [6] are better suited to deal with discontinuous or binary constraints in a GP-based optimization procedure. The binary classifier considers two classes C^+ and C^- over Ω, corresponding to the feasible and unfeasible domains respectively. Each $\mathbf{x}_i$ of $\mathbf{X}_n$ is equipped with a value $z_i = \pm 1$ depending on its membership $C^{\pm}$. To predict the class of a new point $\mathbf{x}$ we introduce a classification function $h : \mathbf{x} \in \Omega \to \mathbb{R}$, such that $z(\mathbf{x}) = \mathrm{sign}h(\mathbf{x})$. A Least-Squares Support Vector Machine (LS-SVM) [42] is used to construct h. The LS-SVM method extends the original Support Vector Machine (SVM) classifier [45] to quadratic penalization, resulting in a linear (but non-sparse) system to be solved (see below). Further details and discussion on SVM and LS-SVM methods can be found in [7].

The LS-SVM method [42] is a linear classifier, for C^+ and C^-, in a feature space induced by the transformation $\boldsymbol{\phi} : \Omega \to \mathcal{F}$:

$$h(\mathbf{x}) = \mathbf{w}^{\mathrm{T}}\boldsymbol{\phi}(\mathbf{x}) + b. \quad (8)$$

Here, $\mathbf{w}$ and $\boldsymbol{\phi}(\mathbf{x})$ are the weights and features vectors, while $b \in \mathbb{R}$ is a constant. The feature space $\mathcal{F}$ is generated by a reproducing kernel $r : \Omega \times \Omega \to \mathbb{R}$ representing the inner product between images in $\mathcal{F}$ of vectors: $r(\mathbf{x}, \mathbf{x}') = \boldsymbol{\phi}(\mathbf{x}) \cdot \boldsymbol{\phi}(\mathbf{x}')$. We use the classical Gaussian kernel,

$$r(\mathbf{x}, \mathbf{x}') = \exp\left(-\frac{\|\mathbf{x} - \mathbf{x}'\|^2}{2\lambda^2}\right), \quad (9)$$

with scale factor $\lambda \in \mathbb{R}$ to be adjusted. The LS-SVM parame-

ters $(\mathbf{w}, b)$ satisfy the primal constrained optimization problem

$$\begin{aligned} \min_{\mathbf{w},b,\mathbf{e}} \quad & \frac{1}{2}\|\mathbf{w}\|^2 + \gamma\frac{1}{2}\sum_{i=1}^{n} e_i^2, \\ \text{s.t.} \quad & z_i = \mathbf{w}^{\mathrm{T}}\boldsymbol{\phi}(\mathbf{x}_i) + b + e_i \quad i = 1,\dots,n, \end{aligned} \tag{10}$$

with trade-off parameter $\gamma \in \mathbb{R}^+$ (to be fixed) and relaxation variables e_i allowing for miss-classification. The Lagrangian of this optimal problem is

$$\begin{aligned} \mathcal{L}(\mathbf{w}, b, \boldsymbol{\alpha}, \mathbf{e}) = & \frac{1}{2}\|\mathbf{w}\|^2 + \gamma\frac{1}{2}\sum_{i=1}^{n} e_i^2 \\ & - \sum_{i=1}^{n} \alpha_i \left(\mathbf{w}^{\mathrm{T}}\boldsymbol{\phi}(\mathbf{x}_i) + b + e_i - z_i\right), \end{aligned} \tag{11}$$

where the $\alpha_i \in \mathbb{R}$ are the Lagrange multipliers of the constraints. Denoting $\mathbf{z} = (z_1 \cdots z_n)^{\mathrm{T}}$, the optimality conditions of the Lagrangian are used to derive a linear system for the dual model parameters b and $\boldsymbol{\alpha} = (\alpha_1 \cdots \alpha_n)^{\mathrm{T}}$,

$$\begin{bmatrix} \mathbf{R} + \gamma^{-1}\mathbf{I} & \mathbf{1} \\ \mathbf{1}^{\mathrm{T}} & 0 \end{bmatrix} \begin{bmatrix} \boldsymbol{\alpha} \\ b \end{bmatrix} = \begin{bmatrix} \mathbf{z} \\ 0 \end{bmatrix}, \tag{12}$$

where $\mathbf{R} \in \mathbb{R}^{n\times n}$ is the kernel matrix with $R_{i,j} = r(\mathbf{x}_i, \mathbf{x}_j)$. This system is solved *via* a Cholesky factorization [7], and h in (8) is expressed in terms of dual model parameters to obtain

$$h(\mathbf{x}) = \sum_{i=1}^{n} \alpha_i r(\mathbf{x}_i, \mathbf{x}) + b. \tag{13}$$

The LS-SVM classifier depends on two parameters, γ and λ, to be fixed when solving (12). We rely on a Leave-One-Out procedure to determine γ and λ that minimize the Predicted Residual Sum-of-Squares (PRESS) criterion [3],

$$\mathrm{PRESS} = \sum_{i=1}^{n} \left(z_i - \widehat{z}_i^{(-i)}\right)^2, \tag{14}$$

where $\widehat{z}_i^{(-i)}$ is the predicted output $z(\mathbf{x}_i)$ of the LS-SVM, when the i-th training point $(\mathbf{x}_i, z_i)$ is disregarded from the construction of the classifier. A simple expression for the predicted residuals is proposed in [8],

$$z_i - \widehat{z}_i^{(-i)} = \frac{\alpha_i}{D_{ii}^{-1}} \quad i = 1,\dots,n, \tag{15}$$

where the D_{ii}^{-1} are the diagonal entries of the inverse of $\mathbf{D}$, the matrix of system (12). The authors of [8] also provide an explicit expression to compute D_{ii}^{-1} during the factorization of $\mathbf{D}$. The minimization of the PRESS (14) for λ and γ is performed with the CMA-ES algorithm [16].

The LS-SVM binary classifier is finally extended to a probabilistic classification, relating h in (13) to the probability of the class C^+, denoted $P(C^+|\mathbf{x})$. A comparison of several probability models for the LS-SVM classification is provided in [43]. We use the sigmoid function [33] and expressing the probability of C^+ as

$$P\left(C^+|\mathbf{x}\right) = \frac{1}{1 + \exp\left(Ah(\mathbf{x}) + B\right)}. \tag{16}$$

The parameters A and B of the sigmoid are determined by minimizing the probability of misclassification, see [33, 25]. In practice, the probability P goes to 1 (resp. 0) as the classifier is certain that $\mathbf{x}$ is feasible and belongs to C^+ (resp. unfeasible and belongs to C^-), while a value of $P = 1/2$ denotes a complete uncertainty in the classification. This can occur because $\mathbf{x}$ is far from any observations in $\mathbf{X}_n$ or close to the interface between the two classes.

Following [38] and [6], the probability of feasibility is used to derive from the AEI a merit function and select a new point $\mathbf{x}_{n+1}$ that yields the highest expected improvement while having a high probability of feasibility. To this end, the authors of [6] use a modified version of the sigmoid function in (16) that accounts for the distances to the closest classified observations (in $\mathbf{X}_n$). While improving the misclassification rate, this modification results in a discontinuous merit function which prevents the use of gradient-based optimization tools to determine $\mathbf{x}_{n+1}$. Further, their strategy requires the addition of $d+1$ new observation points per iteration (to maintain isotropy in the observation points distribution) with an associated cost deemed too important in our application. Instead, we consider a sequential infilling strategy, selecting alternatively one of the following definitions for $\mathbf{x}_{n+1}$:

$$\mathbf{x}_{n+1} = \arg\max_{\mathbf{x}\in\Omega} AEI(\mathbf{x}) P(C^+|\mathbf{x}), \tag{17}$$

$$\mathbf{x}_{n+1} = \arg\min_{\mathbf{x}\in\Omega} \widehat{\mathcal{P}}_n(\mathbf{x}) \quad \text{s.t. } P(C^+|\mathbf{x}) \geq \rho, \tag{18}$$

$$\mathbf{x}_{n+1} = \arg\max_{\mathbf{x}\in\Omega} \left[AEI(\mathbf{x}) P(C^+|\mathbf{x}) \left(1 - P(C^+|\mathbf{x})\right)\right]. \tag{19}$$

The first definition in (17) corresponds to the extension of the AEI favoring points with high chance of feasibility. The second expression (18) directly minimizes the predicted objective, but enforcing a minimal probability ρ of feasibility; we use $\rho = 0.5$. Finally (19) combines the feasibility and infeasibility probabilities to favor areas where the classification is the most uncertain ($P \sim 0.5$), with the objective to improve the exploration of the feasible domain boundaries. In practice, the new points $\mathbf{x}_{n+1}$ are determined using CMA-ES algorithms without [16] or with constraints [4], depending on the considered definition.

As a final note, we remark that the optimization procedure can generate points that are found unfeasible in the sense that $\mathcal{P}(\mathbf{x}_{n+1})$ cannot be computed. This is typically the case when $\mathbf{x}_{n+1}$ corresponds to an impossible geometrical configuration, or to an extreme situation for which the numerical code is not able to converge. It that case, the point is deemed infeasible, setting $z_{n+1} = -1$, but no value of the objective function is provided and the construction of the GP model for $\mathcal{P}$ simply disregard the missing data. As a result, the GP model of $\mathcal{P}$ and the LS-SVM classification can involve different numbers of observations.

3 HYDROFOIL OPTIMIZATION SETUP

This Section introduces the formulation of the constrained optimization problem for the flexible hydrofoil, as defined in collaboration with GTF. Note that some details of the optimization problem are omitted for confidentiality reasons. We

also briefly discuss the fluid and structural solvers used in this work.

3.1 PROBLEM FORMULATION

The optimization of the hydrofoil uses control variables $\mathbf{x}$ which parameterize the geometry of the hydrofoil at rest and the elastic element that gives flexibility to the trailing edge. The optimization concerns the minimization of the hydrofoil drag force over a set of 4 sailing conditions, with an additional set of 4 constraints designed to prevent the cavitation of the flow. Each condition corresponds to a prescribed boat speed and an hydrodynamic lift force developed by the hydrofoil. Note that the 4 drag points and the 4 constraints correspond to different conditions so the evaluation of the objective function $\mathcal{P}$ and the vector of constraints $\mathbf{Q}$ at given $\mathbf{x}$ requires solving 8 fluid-structure interaction problems. The optimization problem is written as

$$\begin{aligned} \min_{\mathbf{x}\in\Omega} \quad & \mathcal{P}(\mathbf{x}) = \sum_{i=1}^{4} w_i \mathrm{C_{d_i}}(\mathbf{x}), \\ \text{s.t.} \quad & \begin{cases} Q_1(\mathbf{x}) = -\mathrm{Cp_{min_1}}(\mathbf{x}) \leq \lambda_1 \\ Q_2(\mathbf{x}) = -\mathrm{Cp_{min_2}}(\mathbf{x}) \leq \lambda_2 \\ Q_3(\mathbf{x}) = -\mathrm{Cp_{min_3}}(\mathbf{x}) \leq \lambda_3 \\ Q_4(\mathbf{x}) = -\mathrm{Cp_{min_4}}(\mathbf{x}) \leq \lambda_4 \end{cases} . \end{aligned} \tag{20}$$

Here, the $\mathrm{C_{d_i}}$ are the drag force coefficients, the $w_i > 0$ are prescribed weights, the $\mathrm{Cp_{min_i}}$ are the minimum pressure coefficients, and the λ_i are the cavitation numbers defined by

$$\lambda = \frac{p_0 - p_v}{\frac{1}{2}\rho U_0^2}. \tag{21}$$

We have denoted U_0 and p_0 the reference velocity (that is, the BS) and pressure, ρ the fluid density, and p_v the saturated vapor pressure. The reference pressure is taken as $p_0 = p_{\mathrm{atm}} + \rho g h$, where p_{atm} is the atmospheric pressure, g is the gravity acceleration, and h is the immersion depth of the hydrofoil. The minimum of the pressure coefficient is defined by $\mathrm{Cp_{min}} = \frac{p_{\min} - p_0}{0.5\rho U_0^2}$, where $p_{\min}$ is the minimal pressure over the hydrofoil surface. The simplest criterion to prevent cavitation is to ensure that the minimal pressure remains higher than the vapor pressure: $p_{\min} \geq p_v$. This condition can be expressed in terms of cavitation number λ to obtain the conditions on $\mathrm{Cp_{min}}$ to formulate the constraints in (20).

3.2 OPTIMIZATION PARAMETERS

For the optimization of the flexible hydrofoil, we started from the baseline geometry previously optimized by GTF. This geometry was obtained using an evolutionary method [5]. The shape of this hydrofoil was parameterized by a set of control points supporting B-Splines basis functions [32]. Two sets of 20 control points were used to represent the upper and lower hydrofoil sides using a fitting technique inspired from [46].

For the results presented in this paper, we decided to reduce the set of geometric parameters in the following way. First, the optimization is made only for the rear part of the hydrofoil, the geometry of the leading part being kept the same as the baseline hydrofoil along up to 70% of the chord length. The forward part of the flexible hydrofoil is considered perfectly rigid in the following. Second, the rear part of the unloaded geometry is defined by rotating the sections of the baseline hydrofoil by an angle $\mathrm{p}(s)$, where s is the reduced coordinate along the chord of the baseline geometry. In practice, the rotation is applied to the original control points of the baseline geometry having $s > 0.7$; the rotation rule $\mathrm{p}(s)$ itself is specified using an additional B-Spline approximation based on 4 control points with $0.7 < s_1 < \cdots < s_4 = 1$ and having rotation angle $\mathrm{p_1}$ to $\mathrm{p_4}$. The B-Spline approximation of $\mathrm{p}(s)$ ensures a smooth connection between the deformed rear and forward parts of the unloaded flexible geometry. The whole procedure is illustrated in Figure 1. In the following, we shall

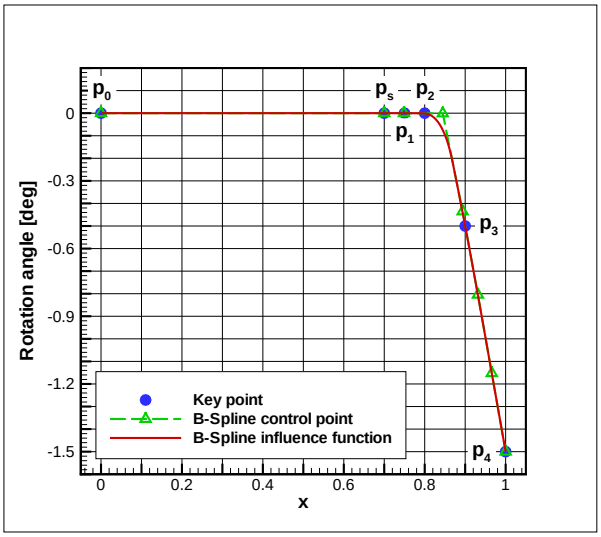

(a) B-Spline approximation of the rotation angle.

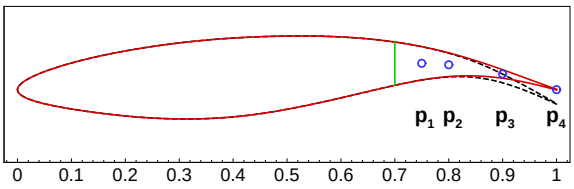

(b) Initial and deformed hydrofoils.

Figure 1: Illustration of the unloaded geometry definition using a rotation of the baseline geometry. The top plot shows the B-Spline approximation of the rotation rule $\mathrm{p}(s)$ based on the rotation angles $\mathrm{p_1}$ to $\mathrm{p_4}$ at the control points. The bottom plot compares the baseline (red) and unloaded flexible geometries, the green vertical line indicating the chord position $s = 0.7$.

refer to the angles $\mathrm{p}_{1,\ldots,4}$ as the 4 geometrical parameters of the optimization problem.

The flexibility of the hydrofoil is obtained by inserting a deformable element between the rigid forward part and the trailing edge. The geometry of this element is defined using its starting and ending points, expressed in chord length coordinates before rotation, on the lower ($\mathrm{s_1}$ and $\mathrm{s_2}$) and upper ($\mathrm{ds_1}$ and $\mathrm{ds_2}$) sides; this coordinates are illustrated in in Figure 2. This deformable element is assumed to be made of

an homogeneous material having a Young modulus $\mathrm{E_{LST}}$; it is further reinforced by a beam (shown in black in Figure 2) on the pressure surface (upper side). The elastic beam has a Young modulus varying linearly between $\mathrm{s_1}$ and $\mathrm{s_2}$ with mean $\mathrm{E_{Beam}}$ and slope $\mathrm{C_{Beam}}$. Overall, the parametrization of the deformable part involves 7 parameters (4 geometric and 3 related to the elastic properties) globally referred to as the structural parameters. Adding together the structural and geometrical parameters makes the optimization variables $\mathbf{x}$.

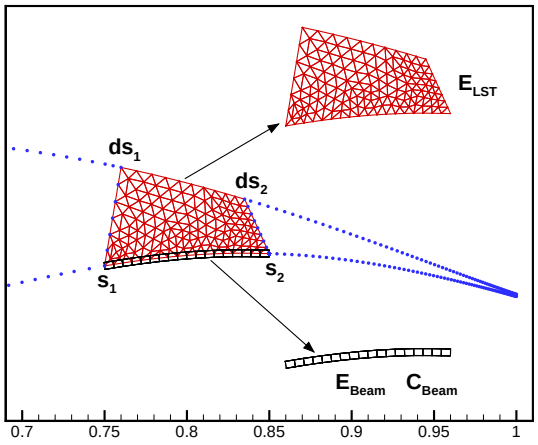

Figure 2: Illustration of the structural parameters.

3.3 FLUID STRUCTURE INTERACTION SOLVER

Given the value of the optimization parameters $\mathbf{x}$, the evaluation of the objective function and the constraints of the optimization calls for the resolution of several FSI problems (as many problems as the set of conditions). We assume that these problems have steady solutions for all values of the design parameters and we rely on a quasi-steady approach to treat the coupling between the structural and fluid solvers.

For the flow solver, we rely on XFOIL [10] which has been developed for many years and is widely used for many aerodynamic applications. While based on a two-dimensional airfoil panel code method, XFOIL can provide viscous and inviscid analyses. It incorporates a two-equation integral formulation of the viscous boundary layer and the approximate e^N envelope method [44]; it allow the prediction of transition points and separation bubble, through the resolution of the boundary layer and the transition equations which is based on a Newton method. Further details on XFOIL are given in [10] and it is compared with other CFD methods and solvers in [28]. We only mention that the setting of our optimization problem imposes to enforce a prescribed lift force in the flow computation. This is achieved in XFOIL by determining the Angle of Attack (AoA) that yields the requested lift force. Overall, XFOIL is simple to use and has a reasonable computation cost on a classical workstation, in most of the cases, making it a natural candidate to be coupled with a structural solver (see for instance [26] for a recent FSI study of a wind turbine blades using XFOIL).

The ARA software developed by K-EPSILON was used to solve the structural model of the flexible trailing edge. The solver was originally developed for FSI computations of sails [13] and proposes various structural elements [12]. In this work, the elastic part of the trailing edge is modeled by 2D Linear Strain Triangles (LST) [31] and Timoshenko beam elements (see Figure 2). The nonlinear equilibrium solution is computed by a Newton method with Aitken relaxation.

A quasi-monolithic algorithm [12] is finally applied to couple the structural and flow solvers. Briefly, in this algorithm, the resolution of the structural problem is nested inside the iterations of the nonlinear steady flow solver. This approach preserves the convergence rate and stability properties of the monolithic approach. The resulting coupled solver is finally driven by a utility that computes the set of FSI solutions required to estimate the objective function value and its constraints (20). This utility is itself nested into the optimization driver that decides of the sequence of new optimal points $\mathbf{x}_{n+1}$ to be evaluated.

4 RESULTS AND DISCUSSIONS

We now present the results of the optimization problem. In particular, we contrast the optimal flexible hydrofoil with its rigid counterpart optimized considering the same set of conditions and constraints. This comparison concerns the characteristics and performances of the two optimal hydrofoils. We do not provide a comparison in terms of computational times because the two optimizations use different strategies and have significantly different complexities. Indeed, the optimization of the rigid hydrofoil although involving a larger number of optimization variables has an objective function and constraints much faster to compute than in the flexible case (which requires the resolution of FSI problems) enabling the application of evolutionary-based methods [5].

In the following, the rigid hydrofoil corresponds to the first initial baseline geometry optimized by GTF, assuming a perfectly rigid hydrofoil. The unloaded flexible one has been optimized after 3 back and forth with GTF, by including imposed flap angles that are function of the BS, in the GTF baseline hydrofoil optimization procedure. The flap angles correspond to the optimal flexible trailing edge law.

4.1 SELECTION OF THE DESIGN VARIABLES

Still, the computational time for the optimization of the flexible hydrofoil is an important aspect, and several tests were made to determine an appropriate trade-off between the computational and parametrization complexities, before arriving at the set-up described in the previous Section 3.2 with the 11 optimization variables. For instance, one can fix the optimization variables related to the material properties, or the geometry of the deformable element, or introduce more control points in the parametrization of the rotation rule, with different complexities of the optimization problem and different computational times as a result. However, limiting the number of optimization variables also impact the performance of the optimal design. Without reporting all of our tests, we simply illustrate here the effect of varying the dimensionality of the

optimization domain. Figure 3 shows the evolutions with the computational time of the estimated minimum of the objective function when considering different numbers of optimization variables. The plot shows that the optimization problem with nine variables needs ≈ 16 times more resources to converge, compared to the case of five optimization variables, with close optimal objectives in the two cases. The case with just two optimization variables is even less computationally demanding but leads to a more noticeable drop in the performance at the optimum.

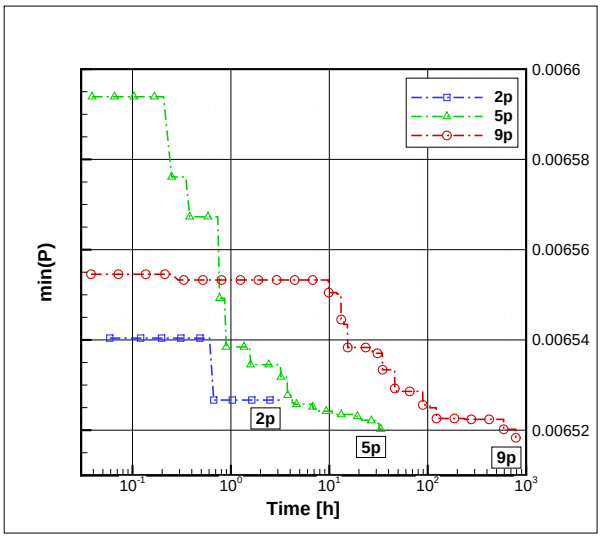

Figure 3: Convergence of the objective function minimum with the computational time, for different numbers of optimization variables.

4.2 OPTIMAL SHAPES AND PRESSURE DISTRIBUTIONS

Figures 4 and 5 show for 20 and 40 kts BS respectively, the shapes of the rigid and flexible hydrofoils. These shapes are depicted at their effective AoA giving the prescribed lift force. The pressure coefficient distributions are also reported in the top part of the Figures. At low BS (20 kts), in Figure 4, the rigid and deformed shapes are seen to be not much different; the rigid one has a higher AoA while the flexible one is slightly more cambered. Regarding the Cp distributions, the rigid case presents a minimum at the leading edge of ≈ -2.25, whereas in the flexible case the minimum peaks to $\mathrm{Cp} \approx -1.1$ only, at the same location. This can be explained as a less cambered geometry generally requires a higher AoA to achieve the same lift force, while $\mathrm{Cp_{min}}$ usually increases with the AoA. Anyway, the results indicate a poorer tolerance to cavitation for the rigid hydrofoil in these conditions.

For 40 kts BS, shown in Figure 5, the two AoA are negative and the rigid one presents again the largest deviation from zero AoA. The deformation of the trailing edge is now pronounced, in the flexible case, as it can be appreciated using dashed black contour which corresponds to the unloaded flexible geometry. The trailing edge deflection is ≈ 9.5 deg. The minima of the pressure coefficients are now located approxi-

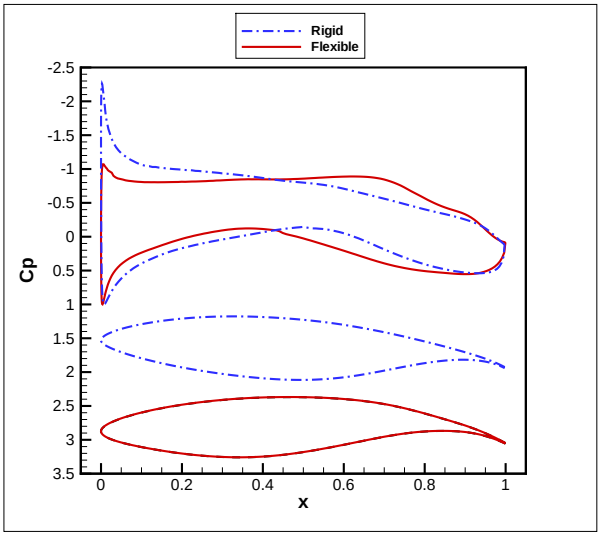

Figure 4: Shapes and distributions of Cp at 20 kts BS for the rigid and flexible hydrofoils.

mately at mid-chord with $\mathrm{Cp_{min}} \approx -0.5$ in the two cases. The distortions in the Cp distribution observed at ≈ 0.8 percent of the chord in the case of the flexible hydrofoil are due to the transitions between the rigid parts and the deformable element constituting the flexible hydrofoil.

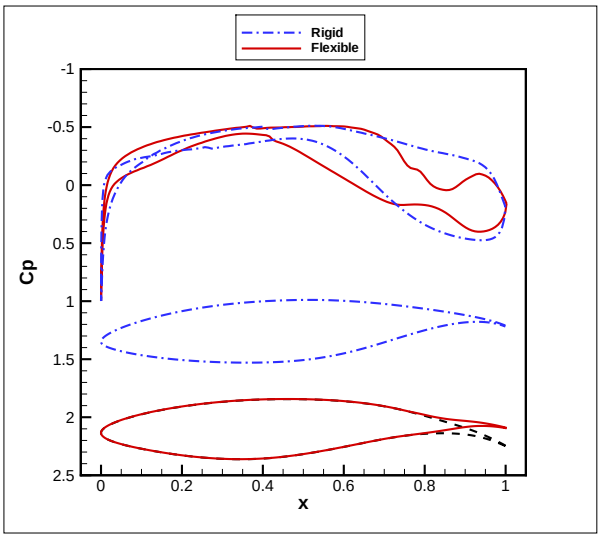

Figure 5: Shapes and distributions of Cp at 40 kts BS for the rigid and flexible hydrofoils.

The flow around the flexible hydrofoil at 40 kts BS has also been computed with a URANS transition model in order to validate the Cp distribution predicted by XFOIL. For that purpose, a structured mesh of the fluid domain around the hydrofoil has been generated using $\approx 110\ 000$ elements; the flow was subsequently solved using FLUENT with the Transition SST turbulence model [27]. The computed pressure coefficient distribution is reported in Figure 6, together with the XFOIL prediction, highlighting the excellent agreement between XFOIL and the Transition SST flow model. Small differences in the Cp are visible only on the pressure side at

$\approx 90\%$ of the chord length, and the magnitude of the differences in the global hydrodynamic loads are 2.6% and 4.2% for the lift and drag coefficients respectively. Thus, the Cp computed by XFOIL can be considered reliable, even in the area of the deformable element.

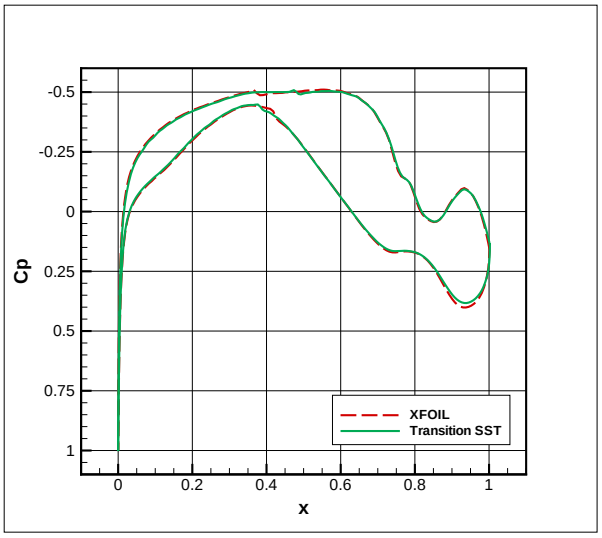

Figure 6: Distributions of Cp predicted by XFOIL and with the URANS transition models.

Figure 7 shows the differences in the thicknesses of the optimal rigid and unloaded flexible hydrofoils. The evolutions of the camber along the chord for the loaded flexible hydrofoil at several BS are also reported. These geometrical quantities are computed based on the distances in the direction normal to the deformed chord, following the classical conventions. Although actual camber and thickness values are not reported, for confidentiality reasons, the differences between the two optimal geometries are evident. Specifically, the flexible hydrofoil in the unloaded configuration is thinner than the rigid one between ≈ 0.3 and 0.9 percent of the chord length. Regarding the camber distribution, the flexibility is seen to have an important effect depending on the BS. In addition, the shapes of the camber distribution of the flexible hydrofoil differ significantly from the rigid one for all the BS shown. Specifically, the maximum camber of the flexible foil at 20 kts BS is more than twice that of the rigid one, while at 40 kts BS it is less by roughly 20%. These evolutions of the apparent camber distribution with the BS (and load in general) is one of the hydrodynamical advantages brought by the flexibility.

4.3 ANGLES OF ATTACK AND CAVITATION CRITERION

The effective AoA of the optimal hydrofoils is reported in Figure 8 as a function of the BS. The previous observations regarding the AoA are confirmed. The AoA of the rigid hydrofoil almost linearly decreases from ≈ 3.9 deg at 20 kts to ≈ -0.9 deg at 30 kts BS, and subsequently continues to decrease, but at a lower rate, when the BS increases further. For the flexible case, the maximum of AoA is only ≈ 1.8 deg at 20 kts and decrease to ≈ -0.1 deg at 25 kts BS. Then, unlike in

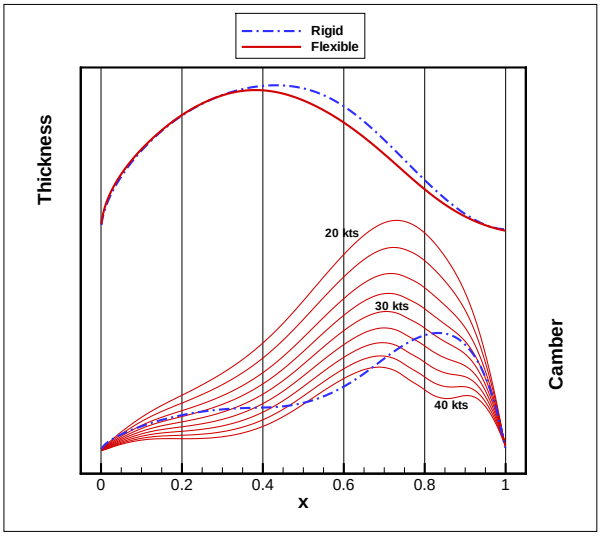

Figure 7: Flexible hydrofoil thickness and camber distributions at several BS. The rigid hydrofoil case is also shown for comparison.

the rigid case, the flexible hydrofoil keeps an almost constant effective AoA between 0 and -1 deg for the rest of BS range, instead of decreasing continuously in the rigid case. Again, the flexibility can explain this behavior, as the deformation of the trailing edge (and reduction of the camber) discharges the foil when the BS increases. This discharge calls for fewer changes in the AoA compared to the rigid case. Note that this sort of automatic trimming, through flexibility, may also be beneficial by saving some trimming efforts to the crew members.

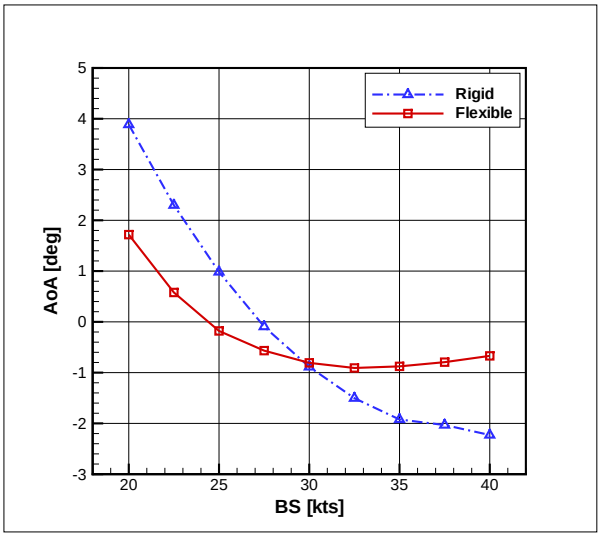

Figure 8: Effective AoA as a function of BS.

Another positive impact of the flexible hydrofoil can be appreciated in Figure 9 which reports the minima of the pressure coefficients $\mathrm{Cp}_{\mathrm{min}}$ for the two optimal hydrofoils, as a function of the BS. The dashed black curve corresponds to the critical value based on the cavitation number (21). We thus expect the optimal hydrofoils to have $\mathrm{Cp}_{\mathrm{min}}$ greater than this

critical value over the whole range of BS considered. However, we recall that the cavitation criterion is enforced for a finite set of only 4 distinct values of the BS. For the maximal BS shown, 40 kts, the two optimal foils, in fact, violate by a small margin the criteria based on the cavitation number, which indeed is not explicitly enforced for this BS. As lower BS are considered, till 25 kts, the two foils satisfy the non-cavitating criterion by a large margin, suggesting that any constraints in this range of BS would not be active. Finally, when the BS approaches 20 kts the behavior of the $\mathrm{Cp_{min}}$ differs between the two hydrofoils: while for the flexible hydrofoil $\mathrm{Cp_{min}}$ remains away from its critical value, it decreases sharply and even becomes significantly lower than its critical value in the rigid case. Comparing the trends of the two hydrofoils, it can be concluded that the flexibility yields a design with $\mathrm{Cp_{min}}$ much less dependent on the BS, and therefore having lower chances of violating the non-cavitating conditions for BS other than in the constraints.

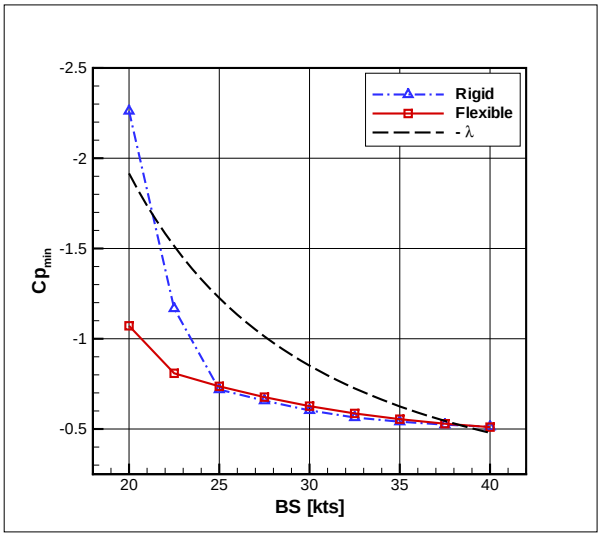

Figure 9: Minimum of pressure coefficients $\mathrm{Cp_{min}}$ as a function of BS. Also shown is the cavitation number λ given by (21).

4.4 DRAG PERFORMANCES

To complete the comparison between the flexible and rigid hydrofoil, we report in Figure 10 the drag coefficients as a function of the BS. The actual values are not shown, for confidentiality reasons, but the plot allows to appreciate the improvement brought by the flexible hydrofoil. Except for the lowest BS (20 kts), the flexible hydrofoil has a drag coefficient $\mathrm{C_d}$ consistently lower than for the rigid one. The improvement is particularly significant at 25 and 40 kts BS, with roughly 20% drag reduction at the highest BS. Again, these improvements come from the flexibility which allows the hydrofoil to naturally adapt its camber with the BS, with a thinner geometry at rest and lower variations of the AoA in the BS range.

For BS between 20 and 25 kts, the hydrofoil drag is mainly depending on the location of the transition point on the suction side, denoted $\mathrm{x_{tr}}$. As the AoA increases to satisfy the

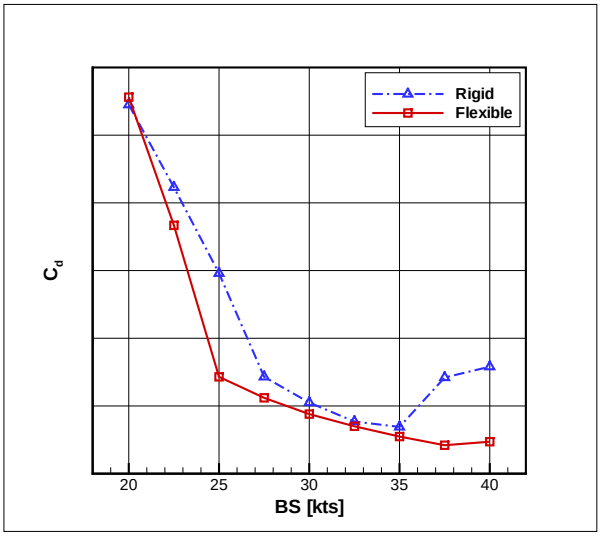

Figure 10: Drag $\mathrm{C_d}$ of the optimal hydrofoils as a function of the BS.

required lift force, $\mathrm{x_{tr}}$ moves toward the leading edge with a sharp increase in the friction drag. Note that in XFOIL the location of the transition point is computed whenever it appears to be in the first 40% of the chord. Otherwise, it is set at this maximal location. To highlight the importance of the transition point on the drag of the hydrofoil, Figure 11 presents the evolutions of the flexible hydrofoil drag and the location of the transition point as functions of the BS. The sharp drop in the hydrofoil drag, around 22.5 kts BS, is clearly related to the displacement of the transition point away from the leading edge. Note that by using different weights and adding more

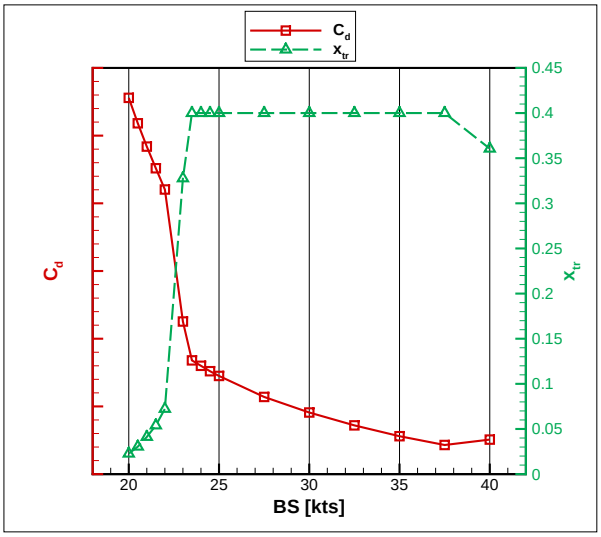

Figure 11: Drag $\mathrm{C_d}$ and transition point location $\mathrm{x_{tr}}$ for the flexible hydrofoil as functions of the BS.

conditions in (20), one could further improve the hydrofoil drag at low BS, by delaying the displacement of the transition point, but to the detriment of the drag at higher BS.

4.5 OPTIMAL HYDROFOIL AT 30 KTS

To illustrate the importance of the selected conditions used in the definition of the objective function, we optimize another rigid hydrofoil based on the minimization of the drag and non-cavitating constraint in (20) based on the unique condition corresponding to 30 kts BS. The design variables are reduced to the 4 geometrical angles $p_{1,\ldots,4}$ and we refer to this optimized hydrofoil as the Rigid 30 kts one.

Table 1 compares the AoA, Cp_{min} and C_d of the flexible and Rigid 30 kts hydrofoils at 30 kts BS. The Rigid 30 kts case has a lower incidence, with a drag reduction of roughly 1.2% compared to the flexible case. The two Cp_{min} are relatively close and far from the criterion based on the cavitation number λ. The closeness of the two hydrofoils at this BS of

	Rigid 30 kts	Flexible	Difference
AoA	$-0.36°$	$-0.81°$	0.55
Cp_{min}	-0.605	-0.627	0.035
C_d	–	–	-0.012

Table 1: Comparison of the hydrodynamical characteristics of the Rigid 30 kts and flexible solutions at 30 kts BS.

30 kts can be further appreciated from Figure 12, where shown are the two distributions of Cp and the shapes plotted at the same AoA for comparison purposes. The main difference in the pressure coefficient is the smoother character of the distribution in the Rigid 30 kts case, which can be explained by the absence of the localized elastic deformations present in the flexible case. However, the differences between the two distributions are small as one could have expected from the similarity of the shapes and effective AoA.

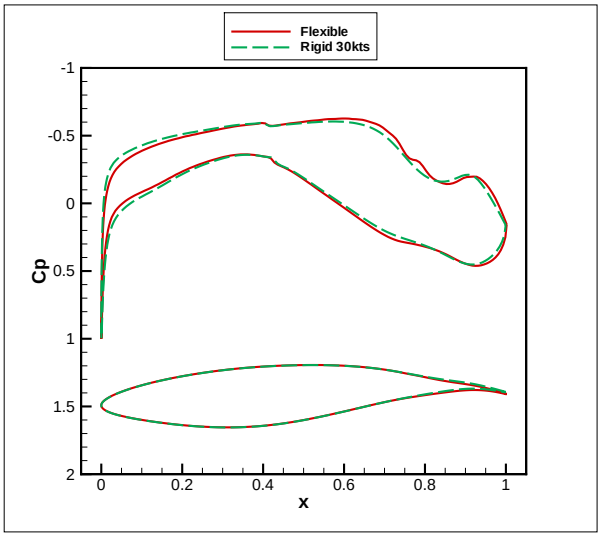

Figure 12: Shapes and Cp distributions for the flexible and Rigid 30 kts solutions at 30 kts BS.

However, as soon as the BS departs from 30 kts, the flexible hydrofoil exhibits a lower drag compared to the Rigid 30 kts one. This can be appreciated in Figure 13 which reports the differences in the drag coefficients, with positive values in favor of the flexible case. Note that these consistent improvements were not necessarily expected as the Rigid 30 kts case does not enforce any non-cavitating conditions at BS other than 30 kts. Therefore, the Rigid 30 kts optimization may have produced a cavitating design with lower drag for other BS. Note also the higher drag for the flexible hydrofoil, at 20 kts BS, where the cavitation criterion is actually not satisfied by the rigid solution.

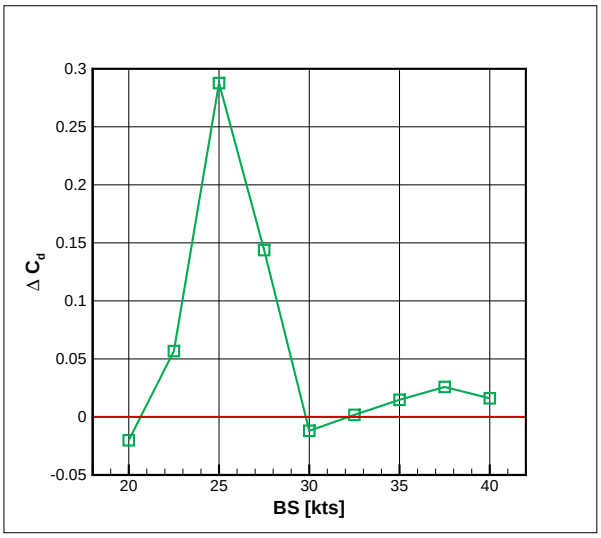

Figure 13: Difference ΔC_d in the drags of the Rigid 30 kts and flexible optima, as a function of the BS.

5 CONCLUSIONS

An advanced multi-design constrained optimization method has been proposed in this paper for the design of a two-dimensional hydrofoil with a flexible trailing edge. Surrogate-model based optimization, with inequality constraints, have been used to enable the optimization of the hydrofoil at a reasonable computational cost. The surrogates are constructed and updated using a limited number of carefully selected resolutions of the fully nonlinear fluid-structure interaction problem. The nonlinear FSI solver used in this work couples a two-dimensional vortex lattice method code for the flow around the hydrofoil with a static structural solver, based on linear stress triangle and Timoshenko beam elements, for the hydrofoil deformations. The optimization involves 4 parameters describing the rotation of a base geometry, and seven elastic parameters describing the properties of the elastic bound between the rigid leading part and trailing edge of the hydrofoil. These parameters are sought to globally minimize the hydrofoil drag forces in selected conditions (boat speeds and lift forces), while constraints were introduced to ensure non-cavitating conditions.

The performances of the resulting optimal flexible hydrofoil have been compared to the rigid case optimized for the same set of conditions. It was found that the flexible hydrofoil performs globally better over the whole set of conditions, compared to the rigid one. In fact, the flexible hydrofoil was found to have drag forces lower than that of the rigid one the

whole range of boat speeds, except around 20 knots where the two cases have essentially the same drag force. The improvement in the drag force brought by the flexibility is particularly noticeable for the highest boat speeds ($\geq$ 35 knots) and around 25 knots. A closer inspection of the optimal solutions revealed that not only the flexible hydrofoil performs better for most conditions, but its angle of attack varies with the boat speed in a tighter range to achieve the prescribed lift conditions, compared to the rigid case. In particular, the flexible hydrofoil has a much smaller angle of attack at low boat speed, which immediately translates into a higher minimum of pressure and less susceptibility to cavitation.

Overall, the optimization clearly evidences the various advantages of considering a hydrofoil with a flexible trailing edge. In particular, it demonstrates that, if correctly designed, the flexible trailing edge allows for an auto-adaption of the hydrofoil camber line and angle of attack with the boat speed, with a global reduction of the drag and lower cavitation risk.

Future developments will concern the optimization of a three-dimensional flexible hydrofoil with the use of more advanced flow models to account for the three-dimensional effects, turbulence, and more complex cavitation criteria. We are currently exploring multi-fidelity strategies [30] to tempered the increase in the computational costs in the three-dimensional case. Another aspect requiring further investigation is the dependence of the transition point displacement as a function of the hydrofoil angle of attack at lower boat speed range. Indeed, we believe that the flexible trailing edge could be effective in producing enough lift for the platform to take off at a lower boat speed.

REFERENCES

[1] Nima Aghajari and Michael Schäfer. Efficient shape optimization for fluid–structure interaction problems. *Journal of Fluids and Structures*, 57:298 – 313, 2015.

[2] Deniz Tolga Akcabay, Eun Jung Chae, Yin Lu Young, Antoine Ducoin, and Jacques André Astolfi. Cavity induced vibration of flexible hydrofoils. *Journal of Fluids and Structures*, 49:463 – 484, 2014.

[3] David M Allen. The relationship between variable selection and data agumentation and a method for prediction. *Technometrics*, 16(1):125–127, 1974.

[4] Dirk V. Arnold and Nikolaus Hansen. A (1+1)-CMA-ES for Constrained Optimisation. In Terence Soule and Jason H. Moore, editors, *GECCO*, pages 297–304, Philadelphia, United States, July 2012. ACM, ACM Press.

[5] T. Bäck and H. P. Schwefel. An Overview of Evolutionary Algorithms for Parameter Optimization. *Evolutionary computation*, 1(1):1–23, 1993.

[6] Anirban Basudhar, Christoph Dribusch, Sylvain Lacaze, and Samy Missoum. Constrained efficient global optimization with support vector machines. *Structural and Multidisciplinary Optimization*, 46(2):201–221, 2012.

[7] Gavin C Cawley. Leave-one-out cross-validation based model selection criteria for weighted ls-svms. In *The 2006 IEEE International Joint Conference on Neural Network Proceedings*, pages 1661–1668. IEEE, 2006.

[8] Gavin C. Cawley and Nicola L.C. Talbot. Efficient leave-one-out cross-validation of kernel fisher discriminant classifiers. *Pattern Recognition*, 36(11):2585 – 2592, 2003.

[9] Olivier Coutier-Delgosha, François Deniset, Jacques André Astolfi, and Jean-Baptiste Leroux. Numerical prediction of cavitating flow on a two-dimensional symmetrical hydrofoil and comparison to experiments. *Journal of Fluids Engineering*, 129(3):279–292, 2007.

[10] Mark Drela. *XFOIL: An Analysis and Design System for Low Reynolds Number Airfoils*, pages 1–12. Springer Berlin Heidelberg, Berlin, Heidelberg, 1989.

[11] Antoine Ducoin, Francois Deniset, Jacques André Astolfi, and Jean-François Sigrist. Numerical and experimental investigation of hydrodynamic characteristics of deformable hydrofoils. *Journal of Ship research*, 53(4):214–226, 2009.

[12] M. Durand. *Interaction fluide-structure souple et légère, application aux voiliers*. PhD Thesis, Ecole Centrale de Nantes, 2012.

[13] M. Durand, A. Leroyer, C. Lothodé, F. Hauville, M. Visonneau, R. Floch, and L. Guillaume. FSI investigation on stability of downwind sails with an automatic dynamic trimming. *Ocean Engineering*, 90:129–139, 2014.

[14] R. Duvigneau and M. Visonneau. Hydrodynamic design using a derivative-free method. *Structural and Multidisciplinary Optimization*, 28(2):195–205, 2004.

[15] Bryan Glaz, Peretz P Friedmann, and Li Liu. Helicopter vibration reduction throughout the entire flight envelope using surrogate-based optimization. *Journal of the American Helicopter Society*, 54(1):12007, 2009.

[16] N. Hansen. The CMA Evolution Strategy: A Comparing Review. In *Towards a new evolutionary computation*, pages 75–102. Springer, 2006.

[17] D. Huang, T. T. Allen, W. I. Notz, and N. Zeng. Global Optimization of Stochastic Black-Box Systems via Sequential Kriging Meta-Models. *Journal of global optimization*, 34(3):441–466, 2006.

[18] Yasuhiko Inukai, Koutarou Horiuchi, Takeshi Kinoshita, Hiromasa Kanou, and Hiroshi Itakura. Development of a single-handed hydrofoil sailing catamaran. *Journal of Marine Science and Technology*, 6(1):31–41, 2001.

[19] Shinkyu Jeong, Mitsuhiro Murayama, and Kazuomi Yamamoto. Efficient optimization design method using kriging model. *Journal of aircraft*, 42(2):413–420, 2005.

[20] D. R. Jones, M. Schonlau, and W. J. Welch. Efficient Global Optimization of Expensive Black-Box Functions. *Journal of Global optimization*, 13(4):455–492, 1998.

[21] Manivannan Kandasamy, Daniele Peri, Seng Keat Ooi, Pablo Carrica, Frederick Stern, Emilio F. Campana, Philip Osborne, Jessica Cote, Neil Macdonald, and Nic de Waal. Multi-fidelity optimization of a high-speed foil-assisted semi-planing catamaran for low wake. *Journal of Marine Science and Technology*, 16(2):143–156, 2011.

[22] Jack P.C. Kleijnen. Kriging metamodeling in simulation: A review. *European Journal of Operational Research*, 192(3):707 – 716, 2009.

[23] Jean-Baptiste Leroux, Olivier Coutier-Delgosha, and Jacques André Astolfi. A joint experimental and numerical study of mechanisms associated to instability of partial cavitation on two-dimensional hydrofoil. *Physics of Fluids*, 17(5), 2005.

[24] W. Li, L. Huyse, and S. Padula. Robust airfoil optimization to achieve drag reduction over a range of mach numbers. *Structural and Multidisciplinary Optimization*, 24(1):38–50, 2002.

[25] Hsuan-Tien Lin, Chih-Jen Lin, and Ruby C. Weng. A note on platt's probabilistic outputs for support vector machines. *Machine Learning*, 68(3):267–276, 2007.

[26] D. MacPhee and Asfaw Beyene. Fluid-structure interaction of a morphing symmetrical wind turbine blade subjected to variable load. *International Journal of Energy Research*, 37(1):69–79, 2013.

[27] Florian R Menter, RB Langtry, SR Likki, YB Suzen, PG Huang, and S Völker. A correlation-based transition model using local variablespart i: model formulation. *Journal of turbomachinery*, 128(3):413–422, 2006.

[28] J. Morgado, R. Vizinho, M.A.R. Silvestre, and J.C. Pscoa. {XFOIL} vs {CFD} performance predictions for high lift low reynolds number airfoils. *Aerospace Science and Technology*, 52:207 – 214, 2016.

[29] Dimitrios I. Papadimitriou and Costas Papadimitriou. Aerodynamic shape optimization for minimum robust drag and lift reliability constraint. *Aerospace Science and Technology*, 55:24 – 33, 2016.

[30] Chanyoung Park, Raphael T. Haftka, and Nam H. Kim. Remarks on multi-fidelity surrogates. *Structural and Multidisciplinary Optimization*, pages 1–22, 2016.

[31] Pauli Pedersen. Some properties of linear strain triangles and optimal finite element models. *International Journal for Numerical Methods in Engineering*, 7(4):415–429, 1973.

[32] Les Piegl and Wayne Tiller. *The NURBS Book (2Nd Ed.)*. Springer-Verlag New York, Inc., New York, NY, USA, 1997.

[33] John C. Platt. Probabilistic outputs for support vector machines and comparisons to regularized likelihood methods. *Advances in large margin classifiers*, 10(3):61–74, 1999.

[34] C. E. Rasmussen and C. K. I. Williams. *Gaussian Processes for Machine Learning*. MIT Press, 2006.

[35] A.F.P. Ribeiro, A.M. Awruch, and H.M. Gomes. An airfoil optimization technique for wind turbines. *Applied Mathematical Modelling*, 36(10):4898 – 4907, 2012.

[36] P.J. Richards, A. Johnson, and A. Stanton. America's cup downwind sails-vertical wings or horizontal parachutes? *Journal of Wind Engineering and Industrial Aerodynamics*, 89(1415):1565 – 1577, 2001. Bluff Body Aerodynamics and Applications.

[37] Matthieu Sacher, Frédéric Hauville, Régis Duvigneau, Olivier Le Maître, Nicolas Aubin, and Mathieu Durand. Efficient optimization procedure in non-linear fluid-structure interaction problem: Application to mainsail trimming in upwind conditions. *Journal of Fluids and Structures*, 69:209 – 231, 2017.

[38] Matthias Schonlau. *Computer Experiments and Global Optimization*. PhD thesis, University of Waterloo, Waterloo, Ont., Canada, Canada, 1997. AAINQ22234.

[39] M. Sedlar, B. Ji, T. Kratky, T. Rebok, and R. Huzlik. Numerical and experimental investigation of three-dimensional cavitating flow around the straight {NACA2412} hydrofoil. *Ocean Engineering*, 123:357 – 382, 2016.

[40] T.W. Simpson, J.D. Poplinski, N. P. Koch, and J.K. Allen. Metamodels for computer-based engineering design: Survey and recommendations. *Engineering with Computers*, 17(2):129–150, 2001.

[41] D.N. Srinath and Sanjay Mittal. Optimal aerodynamic design of airfoils in unsteady viscous flows. *Computer Methods in Applied Mechanics and Engineering*, 199(2932):1976 – 1991, 2010.

[42] J.A.K. Suykens and J. Vandewalle. Least squares support vector machine classifiers. *Neural Processing Letters*, 9(3):293–300, 1999.

[43] Ben Van Calster, Jan Luts, Johan A. K. Suykens, George Condous, Tom Bourne, Dirk Timmerman, and Sabine Van Huffel. *Artificial Neural Networks – ICANN 2007: 17th International Conference, Porto, Portugal, September 9-13, 2007, Proceedings, Part II*, chapter Comparing Methods for Multi-class Probabilities in Medical Decision Making Using LS-SVMs and Kernel Logistic Regression, pages 139–148. Springer Berlin Heidelberg, Berlin, Heidelberg, 2007.

[44] JL Van Ingen. The eN method for transition prediction: historical review of work at tu delft. In *38th Fluid Dynamics Conference and Exhibit*, Seattle, United States, 2008. American Institute of Aeronautics and Astronautics.

[45] Vladimir Vapnik. *The nature of statistical learning theory*. Springer-Verlag New York, Inc., New York, NY, USA, 1995.

[46] Wenping Wang, Helmut Pottmann, and Yang Liu. Fitting b-spline curves to point clouds by curvature-based squared distance minimization. *ACM Trans. Graph.*, 25(2):214–238, 2006.

[47] Qun WEI, Hong xun CHEN, and Rui ZHANG. Numerical research on the performances of slot hydrofoil. *Journal of Hydrodynamics, Ser. B*, 27(1):105 – 111, 2015.